

Event-by-Event Analysis for TeV Electron Candidates with CALET on the International Space Station

Nicholas Cannady^{a,b,c,*}, Yosui Akaike^{d,e} and Shoji Torii^d for the CALET collaboration

^aCenter for Space Sciences and Technology, University of Maryland, Baltimore County, 1000 Hilltop Circle, Baltimore, Maryland 21250, USA

^bAstroparticle Physics Laboratory, NASA/GSFC, Greenbelt, Maryland 20771, USA

^cCenter for Research and Exploration in Space Sciences and Technology, NASA/GSFC, Greenbelt, Maryland 20771, USA

^dWaseda Research Institute for Science and Engineering, Waseda University, 17 Kikuicho, Shinjuku, Tokyo 162-0044, Japan

^eJEM Utilization Center, Human Spaceflight Technology Directorate, Japan Aerospace Exploration Agency, 2-1-1 Sengen, Tsukuba, Ibaraki 305-8505, Japan

E-mail: nicholas.w.cannady@nasa.gov

The Calorimetric Electron Telescope (CALET) is a deep electromagnetic calorimeter designed for the measurement of cosmic-ray electrons on the International Space Station. Deployed on the Exposed Facility of the Japanese Experiment Module since August 2015, it observes cosmic-ray electrons with energies up to above 10 TeV and hadrons up to PeV total energies. Above a few TeV, the decrease in the electron flux and increased contamination by protons in the boosted decision tree (BDT) selection introduce challenges to determination of the flux at the highest energies and the search for signatures of nearby accelerators. To address the proton contamination, we apply a dedicated event-by-event analysis to evaluate the likelihood of each candidate event being a real electron or a contaminating proton. In this work, we detail the implementation of the likelihood analysis based on physically motivated shower parameters in the CALET calorimeter. Large simulated electron and proton datasets tailored to the parameters of the observed candidate events are generated and studied to produce a likelihood parameter for the improved rejection of protons. The results are tied to the BDT selection in the flight data analysis and summarized for the currently identified candidate events. Finally, we discuss an expansion of this work presently under development to use BDTs trained specifically for each candidate to provide an additional figure of merit.

38th International Cosmic Ray Conference (ICRC2023)
26 July - 3 August, 2023
Nagoya, Japan



*Speaker

1. Introduction

The Calorimetric Electron Telescope (CALET) is an International Space Station (ISS)-borne astroparticle physics instrument designed to measure the spectrum of cosmic-ray electrons in the GeV–TeV energy range to search for signatures of nearby sources or dark matter [1]. Deployed on the Japanese Experiment Module Exposed Facility (JEM-EF) since August 2015, CALET has maintained stable data collection for over seven years. These long term observations have improved the statistical significance and reduced the systematic error on the measurement of the electron spectrum up to 4.8 TeV [2]. The obtained spectrum and potential modeling implications are discussed in other submissions to this conference [1–3].

Above these energies, the background contamination of protons into the electron dataset increases, with the relative uncertainty on the flux increasing as a result. In order to probe the residual proton contamination in the electron sample, we apply an event-by-event analysis to determine the relative electron-likeness and proton-likeness of each electron candidate above 4.8 TeV. In this work, we detail the selection of the candidate events, the generation of the dedicated simulations and analysis for each of those candidates, and the results of applying a likelihood method using 13 physically-motivated parameters.

2. Instrument

The CALET calorimeter comprises three main subsystems: the Charge Detector (CHD), the Imaging Calorimeter (IMC), and the Total Absorption Calorimeter (TASC). The CHD contains two layers of 14 plastic scintillating paddles each, arranged for segmentation along the X and Y directions, respectively. The IMC is eight pairs of crossed XY layers of 448 fine scintillating plastic fibers read out with multi-anode photomultipliers (MaPMTs). In order to stimulate first interaction and shower development in the IMC, tungsten sheets are placed between sets of layers such that normal incidence particles have passed three radiation lengths when reaching the last layer. Below the IMC, the TASC contains 12 crossed layers of lead tungstate logs for a total subsystem thickness of 27 radiation lengths. The TASC is able to fully contain electromagnetic showers up to TeV energies, maintaining a fine energy resolution over the operational range of the high energy trigger [4].

3. Event-by-event analysis

We detail in this section the event-by-event analysis applied to the flight data electron candidates, with simulated datasets tailored to each.

3.1 Flight data selection

Electron candidates are chosen using the same criteria for event selection in the standard analysis. The high-energy shower trigger is used [5], which has an approximate low energy threshold for electrons of 10 GeV. A number of pre-selection conditions are applied to isolate well-reconstructed events consistent with electron primaries as detailed below.

- **High-energy offline trigger (OLT)**
We require sufficiently high energy deposits in the bottom layers of the IMC and the top layer of the TASC to avoid inconsistencies between simulated and flight data samples introduced by fluctuations in the hardware trigger thresholds. Fibers in the IMC are routed in pairs of layers in each projection routed into the MaPMTs, such that the sums relevant to the trigger are (IMC X7 + IMC X8) and (IMC Y7 + IMC Y8). We require that each of these sums exceeds 50 minimum-ionizing particle equivalents (MIPs), and that the energy deposit sum in the TASC X1 layer exceeds 100 MIPs.
- **Track quality and geometry**
We use the electromagnetic shower tracking algorithm [6] and require that at least four layers of the IMC are used in each projection of the track. We further require that the reconstructed trajectory falls within the definitions of Geometry A, B, C, or D [7].
- **Shower development cut**
The energy deposits in the bottom layer of the IMC must exceed 10 MIPs to guarantee that the first interaction occurs before the particle reaches the TASC such that the topology of the shower in the IMC can be used for hadron rejection.
- **Shower concentration cut**
The lateral spread of energy deposits in the bottom layer of the IMC is required to be small, such that at least 50% of the total energy deposit in the layer lies within 1 Molière radius (in tungsten) of the reconstructed track.
- **Shower likelihood cut**
A log-likelihood cut is applied using the energy deposits in the IMC and TASC to remove events which are unlike simulated electrons in the same geometric acceptance condition with similar total energy deposits.
- **TASC consistency cut**
The differences between the intersection of the reconstructed track with the midplanes of the top TASC X and Y layers must be less than 2.5 cm to ensure good track quality.
- **Charge cut**
If the CHD is passed through by the reconstructed track, the geometric mean of the hit CHD X and CHD Y paddles must not exceed 3.5 MIPs. If the CHD is not passed through, the energies deposited within 5 fibers of the hit fibers in the first incident IMC X and IMC Y layers must not exceed 3 MIPs each.
- **Boosted Decision Tree (BDT) cut**
A BDT is trained on simulated electron and proton datasets for each geometrical condition and bins of total energy deposited in the TASC. Candidates are chosen if they lie within the 80% containment threshold of the BDT response for electron events. This is the primary discriminant used in the standard electron analysis above ~500 GeV.

3.2 Simulated datasets

The selection as described above yields fewer than 100 candidates in the region above 4 TeV. In order to assess the electron-likeness and proton-likeness of each of these events individually, we require a large sample of electron and proton simulated events which are generated to mimic the flight data event. To this end, we first generate simulated electrons with a throw trajectory given by the reconstructed track in the flight data candidate. The energies of these events are selected to be $\pm 0\%$, $\pm 1\%$, and $+2\%$ of the reconstructed energy of the flight data candidate (dE_{real}). From this relatively small sample, a primary energy (E_p^*) for the simulated electrons is chosen with the highest likelihood to yield the energy deposit sum seen in the TASC for the candidate, which is then used for the generation of the large scale electron set.

For the large scale proton set, the throw trajectory is also chosen to match that of the reconstructed track for the flight data candidate. At such high energies, the uncertainty in the track reconstruction is very small, especially given the preselection conditions on number of layers used and TASC consistency. Unlike the electrons, however, the protons must be generated over a large range of energies. We generate protons with primary energies from $1 \times dE_{real}$ to $10^3 \times dE_{real}$ with a power law distribution of index -2.7 to mimic the cosmic-ray proton spectrum at these energies. Events are then selected based on the consistency of the TASC energy deposit in the simulation and dE_{real} . More detail on this energy filter is given in the next section.

The generation of these datasets, especially the protons, is computationally expensive and time consuming. For this work, we have utilized high-performance computing resources at the Institute for Cosmic Ray Research (ICRR) and the NASA Center for Climate Simulation (NCCS). For each candidate event, 10^5 electron events and between 2×10^5 and 1×10^6 proton events were thrown according to the injection directions and energies above. These events are reconstructed to Level 2 data under the same conditions as flight data and extracted into lightweight Data Summary Tables for further analysis.

3.3 Likelihood procedure

For each candidate event, we seek to generate a figure of merit to evaluate the relative likelihood of being an electron vs. a proton. In this analysis, we create a likelihood parameter based on 13 physically motivated shower quantities. These quantities, which are the same used in the latest revision of the BDT for the standard electron analysis, are:

- R_E , the lateral shower width in the TASC. (generally *smaller* for electrons)
- F_E , the fraction of energy deposited in the TASC which is in the bottom layer. (generally *smaller* for electrons)
- C_E , the fraction of energy deposited in the bottom IMC layer which is within 1 Molière radius (for tungsten) of the reconstructed track. (generally *larger* for electrons)
- S_{CHD} , the energy deposit sum in the CHD. (generally *smaller* for electrons)
- TASC fit α/b , the shower maximum in the TASC. (generally *smaller* for electrons)
- TASC fit b , the shower attenuation constant in the TASC. (generally *larger* for electrons)

- TASC fit $T_{5\%}$, the depth at which the cumulative shower energy exceeds 5%.
- TASC fit χ^2/ndf , the goodness of fit for the shower profile.
- IMC fit p_0 , constant in exponential fit of IMC shower profile.
- IMC fit p_1 , slope in exponential fit of IMC shower profile.
- IMC fit χ^2/ndf , the goodness of fit for the shower profile.
- IMC ratio 6 – 7, the ratio of energy deposit in IMC layer 7 to that in IMC layer 6.
- IMC ratio max , the maximum ratio of energy deposits in successive IMC layers in the lower half of the instrument for the event.

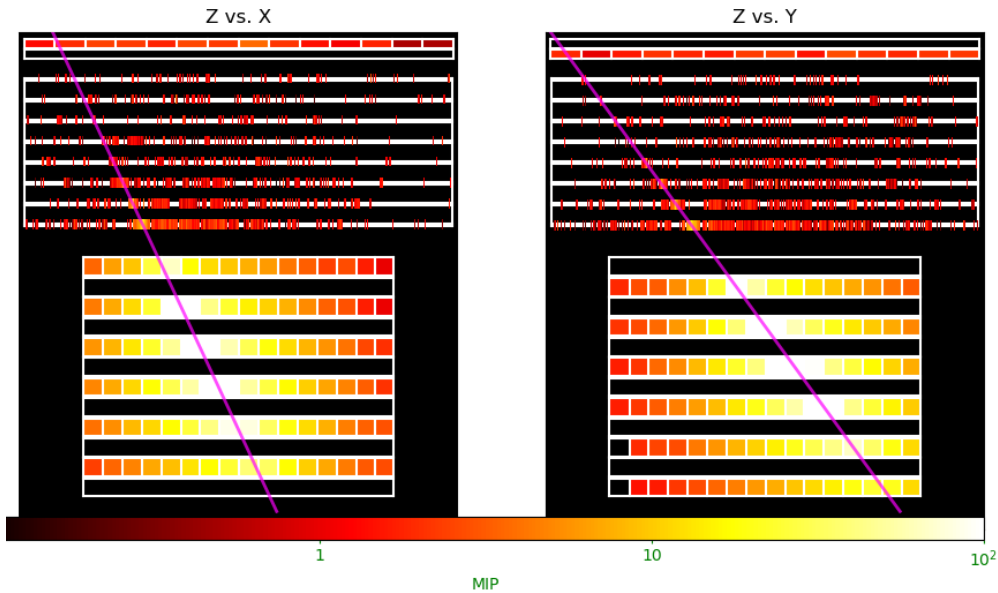


Figure 1: Event viewer display of the candidate event 18041807, which has reconstructed energy 12.04 TeV.

The analysis procedure for each event follows. An example candidate observed on 2018/04/18, as shown in Figure 1, will be used to illustrate at various points.

1. Filter the simulated electron and proton datasets using the same selections as those applied to the flight data to identify electron candidates *except* for the final BDT cut.
2. Further filter the simulated proton dataset to only accept events with energy deposit within 50% of dE_{real} . Energy-deposit dependence of the selection parameters has been evaluated (and found to be small), and the parameters are scaled to correspond to dE_{real} .
3. Fill histograms of each of the 13 parameters above for the simulated electron and proton samples. An example for a representative candidate is shown in Figure 2.

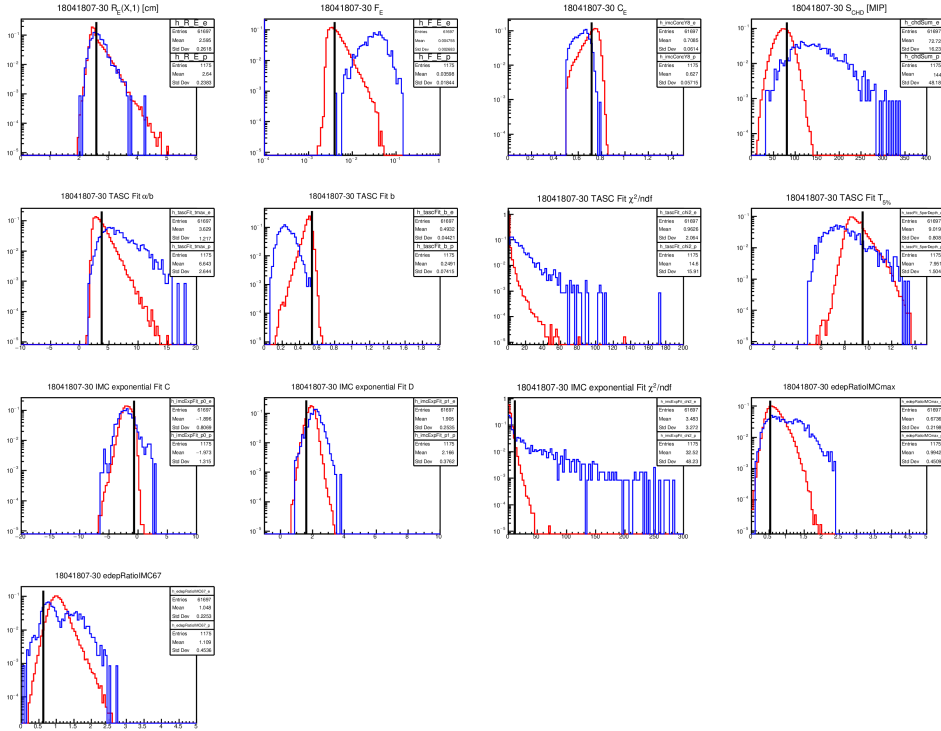


Figure 2: The distributions of the 13 selection parameters for candidate 18041807. Starting from the upper left, the parameters are shown in the order described at the beginning of this section. In each plot, the red curve indicates simulated electrons, the blue curve simulated protons, and the black line the real flight data candidate.

4. Generate distributions of likelihood ratio (LR) for the simulated electron and proton datasets according to

$$LR(k) = \log_{10} \prod_{i=1}^n \frac{p_e^{(k)}(i)}{p_p^{(k)}(i)}, \quad (1)$$

for simulated event k and selection parameter i , such that

$$p_s^{(k)}(i) = \frac{m_s^{(k)}(i)}{m_s^{(tot)}(i)}, \quad (2)$$

where $m_s^{(k)}(i)$ is the number of events in the same bin as event k of the histogram of selection parameter i for species s , and $m_s^{(tot)}(i)$ is the total number of events in that histogram.

5. Calculate the LR for the real candidate event in the same fashion, using the real measured values of the 13 selection parameters.
6. Scale the distributions of LR for the protons, such that the ratio of protons to electrons matches that observed in the flight data template fit of the pre-cut BDT parameters in the energy bin corresponding to the real candidate event.

7. Further scale the distributions of LR for the electrons and protons together (preserving the ratio between the two) such that the sum of simulated electron events with LR equal to or above that of the real candidate event is equal to 1. After this scaling, the integral of the proton distribution with LR equal to or above that of the real candidate event provides the residual proton contamination probability p_{cont} for that candidate. That is to say, for each 1 electron in the electron dataset at the confidence level of the real candidate event, p_{cont} protons are observed. An example of the resulting distributions is shown in Figure 3.
8. In order to avoid underestimation of the proton background due to the paucity of proton events surviving at high values of LR , a Gaussian is fit to the tail of the distribution. The integral of this fit is used as a more conservative estimate of the proton contamination probability.

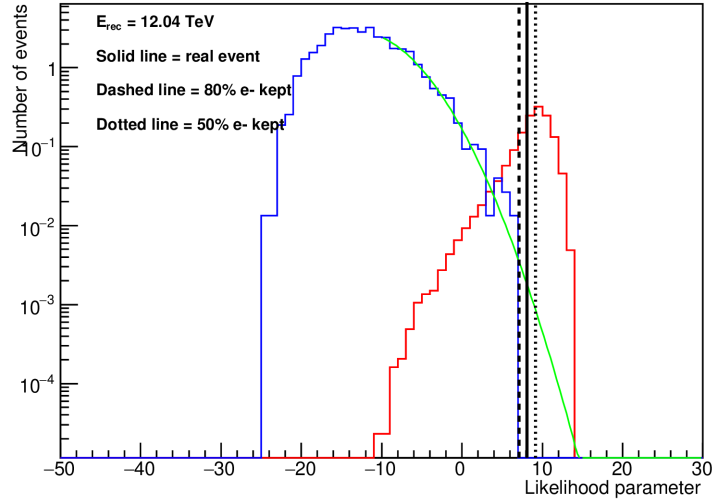


Figure 3: The resulting normalized distributions of likelihood ratios for candidate 18041807. Again in this plot, the red and blue histograms represent the simulated electrons and protons, respectively. The solid black line shows the value of LR for the real candidate event, and the dashed and dotted black lines show the 80% and 50% containment values of LR for electrons, respectively. The green curve shows the Gaussian fit to the tail of the proton distribution.

The renormalization described is intended to relate the value of p_{cont} to the abundances in the standard CALET analysis. It is meaningful due to the identical selections applied to the flight and simulated datasets. It is for this reason—that the template fits of the BDT response distributions are performed before the BDT cut itself is applied—that it is appropriate not to apply a BDT cut to the simulated sample used in the analysis of each candidate.

4. Results

Multiple lists of candidate events have been generated in successive applications of the updates to the electron analysis as new analysis choices are made and more candidates are accumulated. In total, this has yielded 35 candidate events above 4.8 TeV for observations through 2022/12/31.

When restricting the sample to the charge cut as described in the selection above, 23 events remain above 4.8 TeV. Given that the applicability of the scaling based on BDT distribution template fits in the standard analysis is only valid based on these analysis choices, we report here on those events only. A number of the events above 4.8 TeV, including the example event shown from 2018/04/18, are identified as high-fidelity electron candidates and the implications for modeling will be reported in an upcoming publication.

5. Conclusion

We reported here on a likelihood-based analysis of individual electron candidates at high energies with CALET. We have applied this method to a sample of events and identified high-fidelity electron candidates above 4.8 TeV. Extensions of this analysis are underway, including testing results under variation of the charge cut used in the standard analysis. In addition, the possibility of a BDT-based approach trained for each event separately is being explored to better weight the varying separation power of each of the parameters used in the analysis. As CALET is approved through the end of 2024 (and hopefully beyond) and continues healthy scientific data collection, we anticipate further application of this procedure to new candidate events.

Acknowledgements

We gratefully acknowledge JAXA's contributions to the development of CALET and to the operations onboard the International Space Station. The CALET effort in Italy is supported by ASI under Agreement No. 2013-018-R.0 and its amendments. The CALET effort in the United States is supported through Grants No. 80NSSC20K0397, No. 80NSSC20K0399, and Np. NNH18ZDA001N-APRA18-004, and under award Np. 80GSFC21M0002. This work was supported in part by JSPS Grant-in-Aid for Scientific Research (S) Grant No. 19H05608 in Japan.

References

- [1] S. Torii for the CALET Collaboration, "Highlights from the CALET observations for 7.5 years on the International Space Station," this conference.
- [2] Y. Akaike for the CALET Collaboration, "The cosmic-ray electron and positron spectrum measured with CALET on the International Space Station," this conference.
- [3] H. Motz for the CALET Collaboration, "Interpretation of the CALET Electron+Positron Spectrum by Astrophysical Sources," this conference.
- [4] Y. Asaoka et al. (CALET Collaboration), "Energy Calibration of CALET Onboard the International Space Station," AP 91, 1–10 (2017).
- [5] Y. Asaoka et al. (CALET Collaboration), "On-Orbit Operations and Offline Data Processing of CALET Onboard the ISS," AP 100, 29–37 (2018).
- [6] Y. Akaike for the CALET Collaboration, "CALET observational performance expected by CERN beam test," in PoS (ICRC2013) 726 (2013).
- [7] O. Adriani et al. (CALET Collaboration), "Extended Measurement of the Cosmic-Ray Electron and Positron Spectrum from 11 GeV to 4.8 TeV with the Calorimetric Electron Telescope on the International Space Station," PRL 120, 261102 (2018).

Full Author List: CALET Collaboration

O. Adriani^{1,2}, Y. Akaike^{3,4}, K. Asano⁵, Y. Asaoka⁵, E. Berti^{2,6}, G. Bigongiari^{7,8}, W.R. Binns⁹, M. Bongi^{1,2}, P. Brogi^{7,8}, A. Bruno¹⁰, N. Cannady^{11,12,13}, G. Castellini⁶, C. Checchia^{7,8}, M.L. Cherry¹⁴, G. Collazuol^{15,16}, G.A. de Nolfo¹⁰, K. Ebisawa¹⁷, A.W. Ficklin¹⁴, H. Fuke¹⁷, S. Gonzi^{1,2,6}, T.G. Guzik¹⁴, T. Hams¹¹, K. Hibino¹⁸, M. Ichimura¹⁹, K. Ioka²⁰, W. Ishizaki⁵, M.H. Israel⁹, K. Kasahara²¹, J. Kataoka²², R. Kataoka²³, Y. Katayose²⁴, C. Kato²⁵, N. Kawanaka²⁰, Y. Kawakubo¹⁴, K. Kobayashi^{3,4}, K. Kohri²⁶, H.S. Krawczynski⁹, J.F. Krizmanic¹², P. Maestro^{7,8}, P.S. Marrocchesi^{7,8}, A.M. Messineo^{8,27}, J.W. Mitchell¹², S. Miyake²⁸, A.A. Moiseev^{29,12,13}, M. Mori³⁰, N. Mori², H.M. Motz¹⁸, K. Munakata²⁵, S. Nakahira¹⁷, J. Nishimura¹⁷, S. Okuno¹⁸, J.F. Ormes³¹, S. Ozawa³², L. Pacini^{2,6}, P. Papini², B.F. Rauch⁹, S.B. Ricciarini^{2,6}, K. Sakai^{11,12,13}, T. Sakamoto³³, M. Sasaki^{29,12,13}, Y. Shimizu¹⁸, A. Shiomi³⁴, P. Spillantini¹, F. Stolzi^{7,8}, S. Sugita³³, A. Sulaj^{7,8}, M. Takita⁵, T. Tamura¹⁸, T. Terasawa⁵, S. Torii³, Y. Tsunesada^{35,36}, Y. Uchihori³⁷, E. Vannuccini², J.P. Wefel¹⁴, K. Yamaoka³⁸, S. Yanagita³⁹, A. Yoshida³³, K. Yoshida²¹, and W.V. Zober⁹

¹Department of Physics, University of Florence, Via Sansone, 1 - 50019, Sesto Fiorentino, Italy, ²INFN Sezione di Firenze, Via Sansone, 1 - 50019, Sesto Fiorentino, Italy, ³Waseda Research Institute for Science and Engineering, Waseda University, 17 Kikuicho, Shinjuku, Tokyo 162-0044, Japan, ⁴JEM Utilization Center, Human Spaceflight Technology Directorate, Japan Aerospace Exploration Agency, 2-1-1 Sengen, Tsukuba, Ibaraki 305-8505, Japan, ⁵Institute for Cosmic Ray Research, The University of Tokyo, 5-1-5 Kashiwa-no-Ha, Kashiwa, Chiba 277-8582, Japan, ⁶Institute of Applied Physics (IFAC), National Research Council (CNR), Via Madonna del Piano, 10, 50019, Sesto Fiorentino, Italy, ⁷Department of Physical Sciences, Earth and Environment, University of Siena, via Roma 56, 53100 Siena, Italy, ⁸INFN Sezione di Pisa, Polo Fibonacci, Largo B. Pontecorvo, 3 - 56127 Pisa, Italy, ⁹Department of Physics and McDonnell Center for the Space Sciences, Washington University, One Brookings Drive, St. Louis, Missouri 63130-4899, USA, ¹⁰Heliospheric Physics Laboratory, NASA/GSFC, Greenbelt, Maryland 20771, USA, ¹¹Center for Space Sciences and Technology, University of Maryland, Baltimore County, 1000 Hilltop Circle, Baltimore, Maryland 21250, USA, ¹²Astroparticle Physics Laboratory, NASA/GSFC, Greenbelt, Maryland 20771, USA, ¹³Center for Research and Exploration in Space Sciences and Technology, NASA/GSFC, Greenbelt, Maryland 20771, USA, ¹⁴Department of Physics and Astronomy, Louisiana State University, 202 Nicholson Hall, Baton Rouge, Louisiana 70803, USA, ¹⁵Department of Physics and Astronomy, University of Padova, Via Marzolo, 8, 35131 Padova, Italy, ¹⁶INFN Sezione di Padova, Via Marzolo, 8, 35131 Padova, Italy, ¹⁷Institute of Space and Astronautical Science, Japan Aerospace Exploration Agency, 3-1-1 Yoshinodai, Chuo, Sagamihara, Kanagawa 252-5210, Japan, ¹⁸Kanagawa University, 3-27-1 Rokkakubashi, Kanagawa, Yokohama, Kanagawa 221-8686, Japan, ¹⁹Faculty of Science and Technology, Graduate School of Science and Technology, Hirosaki University, 3, Bunkyo, Hirosaki, Aomori 036-8561, Japan, ²⁰Yukawa Institute for Theoretical Physics, Kyoto University, Kitashirakawa Oiwake-cho, Sakyo-ku, Kyoto, 606-8502, Japan, ²¹Department of Electronic Information Systems, Shibaura Institute of Technology, 307 Fukasaku, Minuma, Saitama 337-8570, Japan, ²²School of Advanced Science and Engineering, Waseda University, 3-4-1 Okubo, Shinjuku, Tokyo 169-8555, Japan, ²³National Institute of Polar Research, 10-3, Midori-cho, Tachikawa, Tokyo 190-8518, Japan, ²⁴Faculty of Engineering, Division of Intelligent Systems Engineering, Yokohama National University, 79-5 Tokiwadai, Hodogaya, Yokohama 240-8501, Japan, ²⁵Faculty of Science, Shinshu University, 3-1-1 Asahi, Matsumoto, Nagano 390-8621, Japan, ²⁶Institute of Particle and Nuclear Studies, High Energy Accelerator Research Organization, 1-1 Oho, Tsukuba, Ibaraki, 305-0801, Japan, ²⁷University of Pisa, Polo Fibonacci, Largo B. Pontecorvo, 3 - 56127 Pisa, Italy, ²⁸Department of Electrical and Electronic Systems Engineering, National Institute of Technology (KOSEN), Ibaraki College, 866 Nakane, Hitachinaka, Ibaraki 312-8508, Japan, ²⁹Department of Astronomy, University of Maryland, College Park, Maryland 20742, USA, ³⁰Department of Physical Sciences, College of Science and Engineering, Ritsumeikan University, Shiga 525-8577, Japan, ³¹Department of Physics and Astronomy, University of Denver, Physics Building, Room 211, 2112 East Wesley Avenue, Denver, Colorado 80208-6900, USA, ³²Quantum ICT Advanced Development Center, National Institute of Information and Communications Technology, 4-2-1 Nukui-Kitamachi, Koganei, Tokyo 184-8795, Japan, ³³College of Science and Engineering, Department of Physics and Mathematics, Aoyama Gakuin University, 5-10-1 Fuchinobe, Chuo, Sagamihara, Kanagawa 252-5258, Japan, ³⁴College of Industrial Technology, Nihon University, 1-2-1 Izumi, Narashino, Chiba 275-8575, Japan, ³⁵Graduate School of Science, Osaka Metropolitan University, Sugimoto, Sumiyoshi, Osaka 558-8585, Japan, ³⁶Nambu Yoichiro Institute for Theoretical and Experimental Physics, Osaka Metropolitan University, Sugimoto, Sumiyoshi, Osaka 558-8585, Japan, ³⁷National Institutes for Quantum and Radiation Science and Technology, 4-9-1 Anagawa, Inage, Chiba 263-8555, Japan, ³⁸Nagoya University, Furo, Chikusa, Nagoya 464-8601, Japan, ³⁹College of Science, Ibaraki University, 2-1-1 Bunkyo, Mito, Ibaraki 310-8512, Japan